

Key Points:

- The convective mergers and the associated lightning surge are well simulated by Weather Research and Forecasting coupled with an explicit electrification scheme
- During the merger, a stronger updraft center is generated near the cloud bridge, producing a large number of new graupel and snow here
- The rapid increase and redistribution of ice-phase particles form a five-layer charge structure, intensifying the vertical electrical field

Correspondence to:

X. Qie and X. Xiao,
qie@mail.iap.ac.cn;
xxiao@ium.cn

Citation:










Lu, J., Qie, X., Xiao, X., Jiang, R., Mansell, E. R., Fierro, A. O., et al. (2022). Effects of convective mergers on the evolution of microphysical and electrical activity in a severe squall line simulated by WRF coupled with explicit electrification scheme. *Journal of Geophysical Research: Atmospheres*, 127, e2021JD036398. <https://doi.org/10.1029/2021JD036398>

Received 23 DEC 2021
 Accepted 18 JUL 2022

Author Contributions:

Conceptualization: Xiushu Qie, Rubin Jiang
Data curation: Dongfang Wang
Formal analysis: Jingyu Lu, Xian Xiao
Funding acquisition: Xiushu Qie
Investigation: Jingyu Lu
Project Administration: Xiushu Qie, Rubin Jiang
Resources: Xiushu Qie
Software: Edward R. Mansell, Alexandre O. Fierro
Supervision: Xiushu Qie, Rubin Jiang
Visualization: Jingyu Lu
Writing – original draft: Jingyu Lu
Writing – review & editing: Xiushu Qie, Xian Xiao, Rubin Jiang, Edward R. Mansell, Alexandre O. Fierro, Dongxia Liu, Zhixiong Chen, Shanfeng Yuan, Mengyu Sun, Han Yu, Yuxin Zhang, Yoav Yair

Effects of Convective Mergers on the Evolution of Microphysical and Electrical Activity in a Severe Squall Line Simulated by WRF Coupled With Explicit Electrification Scheme

Jingyu Lu^{1,2} , Xiushu Qie^{1,2} , Xian Xiao^{3,4} , Rubin Jiang¹ , Edward R. Mansell⁵ , Alexandre O. Fierro^{5,6,7}, Dongxia Liu¹ , Zhixiong Chen⁸, Shanfeng Yuan¹ , Mengyu Sun^{1,2}, Han Yu¹ , Yuxin Zhang^{1,2}, Dongfang Wang¹, and Yoav Yair⁹ 

¹Key Laboratory of Middle Atmosphere and Global Environment Observation (LAGEO), Institute of Atmospheric Physics, Chinese Academy of Sciences, Beijing, China, ²College of Earth and Planetary Sciences, University of Chinese Academy of Sciences, Beijing, China, ³Institute of Urban Meteorology, China Meteorological Administration, Beijing, China, ⁴Beijing Urban Meteorological Engineering Research Center, Beijing, China, ⁵NOAA/National Severe Storms Laboratory, Norman, OK, USA, ⁶Cooperative Institute for Mesoscale Meteorological Studies, University of Oklahoma, Norman, OK, USA, ⁷Department of Forecasting Models, Zentralanstalt für Meteorologie und Geodynamik (ZAMG), Vienna, Austria, ⁸Key Laboratory for Humid Subtropical Eco-Geographical Processes of the Ministry of Education, School of Geographical Sciences, Fujian Normal University, Fuzhou, China, ⁹School of Sustainability, Interdisciplinary Center (IDC) Herzliya, Herzliya, Israel

Abstract To investigate the process of convective merger (CM) and its effect on thunderstorms evolution and corresponding electrical activity, a severe squall line that took place on 27 July 2015 over the Beijing Metropolitan Region (BMR) is simulated and studied using the Weather Research and Forecasting (WRF) model coupled with an explicit electrification lightning scheme (*E*-WRF). The model-simulated radar reflectivity reasonably captured the whole squall line evolution, including the merging of individual cells and storms. The variation of normalized flash frequency simulated by *E*-WRF is highly consistent with the occurrence of a prominent flash rate surge during the CM both in the observation and the simulation. Cloud bridge is one of the regions where lightning events increase most. The upstream anvil and the sinking outflow led to the rapid connection and formation of new convective cells between the two older main storms. Subsequently, the mass of graupel and snow increased substantially at the middle level, and the mass of upper-level ice was horizontally advected from upstream. During the merger, the in-cloud charge distribution evolved from a staggered charge pocket structure into a vertically stratified five-layer structure. This study supports the hypothesized role of CM in enhancing lightning activity, and further expands our understanding of CM effects on microphysics and charge-redistribution.

1. Introduction

Severe convective thunderstorms, which occur frequently during the warm season, cause significant loss of life and property amounting to several billion RMB in China. Among the threats they carry, lightning activity can be lethal and destructive. Convective merger (CM) is a process in which two or more convective cells or storms merge into a larger storm, then share a common cloud material and dynamical circulation, which is critical for the development, maintenance, and reinforcement of some intense weather systems like thunderstorms, hailstorms, and so on (Krauss et al., 2012; Ping et al., 2014). Storms that have experienced the CMs usually have a longer life cycle (Karacostas et al., 2016; Moseley et al., 2016), and exhibit a more complicated structure (French & Parker, 2012; Knievel & Johnson, 2002; Parker & Johnson, 2004; Romanic et al., 2019), and produce more intense precipitation (Glenn & Krueger, 2017; Sinkevich & Krauss, 2014) than those that have not.

Both observation and simulation studies indicate that the promotion of the cloud system features are due to the influence of CMs on the in-cloud thermodynamic processes (Ping et al., 2014; Zhou et al., 2020). With the upscaling of the cloud, the updraft parcel is less diluted by entrainment with dry air and is therefore more buoyant (Glenn & Krueger, 2017). On another hand, when the CM happens between the storms, their cold pools can collide and deepen, then generate positive feedback by mechanical or thermodynamic lifting, which is the so-called cold pool dynamics (Z. Feng et al., 2015; Haerter & Schlemmer, 2018; Torri et al., 2015; Torri &

Kuang, 2016). These enhanced vertical processes can bring water vapor to higher levels and participate more in the cold-cloud process. Therefore, the CM increases the diameter and thickness of the cloud while possibly producing more ice-phase particles, such as graupel and cloud ice (Bang & Zipser, 2019; Karacostas et al., 2016; Wen et al., 2017). Bang and Zipser (2019) found that oceanic storms that organize or merge into complexes can provide deeper updraft forces to produce graupel and electrification. In addition, there may be some particle transport processes between very close clouds. The video sonde data of the merging cells showed an abundance of large and rapid-growth graupel within a narrow area just above the freezing level in the cloud, which might have been produced through the capture of supercooled droplets transported from upwind cells (Takahashi et al., 2001). Knupp et al. (2003) proposed the hypothesis that the upstream anvil seeding to downstream, leads to the increasing number of lightning in the three tornadic supercells from upstream to downstream.

Since the dynamics and microphysics of storms are greatly influenced by the CM, the intracloud electrification and lightning activities will also be affected (Bringi et al., 1997; G. Feng et al., 2007; MacGorman et al., 2007). A few observational studies have indicated that lightning activity will generally increase rapidly (or jump) following the onset of CM (Carey & Rutledge, 2000; Chen et al., 2020; Gauthier et al., 2010). By examining over 3.8 million convective cells, Gauthier et al. (2010) found a positive correlation between the spatial distribution of CM locations and cloud-to-ground (CG) flashes events. In an electrically active tropical convective complex, Carey and Rutledge (2000) discovered that the merged convective complexes produced 97% of the rainfall and mixed-phase ice mass and 100% of the CG flash events. Lu, Qie, Jiang, et al. (2021) found that a squall line formed through CM between local storms and external storms showed that the total frequency of lightning doubled within 18 min after the CM, due to the vigorous front cells promoted by the advancing rear-inflow jet.

Recent modeling studies suggested that global warming may result in increased surface temperatures, enhanced thermal instability, stronger moisture transport to the upper troposphere, and amplifying cloud-cloud interaction and mergers (Moseley et al., 2016; Tan et al., 2015). Therefore, some studies predict a higher frequency of more intense convective precipitation events (Keller et al., 2018; Lenderink et al., 2017; Moseley et al., 2019; Westra et al., 2014), more frequent lightning events (Chakraborty et al., 2021; K. Qie et al., 2021; Romps et al., 2014) in the future.

Based on these previous studies, the complex range of effects of the CM, such as reduced entrainment, cold pool dynamics, and microphysical influence, may effectively increase the number and collision of different types of ice particles in the mixed-phase layer, thus strengthen the non-induced electrification, and eventually enhance the lightning. It remains a difficult topic to establish a direct relationship between the CM and lightning enhancement according to these speculative factors. While high spatiotemporal resolution meteorological observations and coordinated lightning observations are promising approaches to better identify and quantify these effects, numerical simulations can also serve as a necessary complement to help resolve small-scale processes that are difficult to observe (Fierro et al., 2006; Lagasio et al., 2017; Zheng et al., 2021).

In this study, we investigate the electrical characteristics of a severe squall line and the potential CM enhancement mechanisms of thermodynamics and microphysics. This is achieved using the Weather Research and Forecasting (WRF) model coupled with an explicit in-cloud electrification scheme and a bulk lightning parameterization, referred to as *E*-WRF (Fierro et al., 2013; Sun et al., 2021). The manuscript is organized as follows. Section 2 introduces data and the *E*-WRF model. Section 3 describes the evolution properties of the squall line and its lightning activity. Section 4 validates the simulation by using S-band radar and lightning data. Section 5 presents the thermodynamic and microphysical processes that are associated with the simulated CM-induced lightning surge. Finally, major conclusions and a conceptual diagram of the CM-enhanced mechanism are provided in Section 6.

2. Data, Model, and Method

2.1. Lightning and Other Meteorological Data

The STORM973 (Dynamic-Microphysical-Electrical Processes in Severe Thunderstorms and Lightning Hazards) program provides a data set of thunderstorm observations in the Beijing Metropolitan Region (BMR). STORM973 aims to comprehensively understand the lightning characteristics and relationships between lightning activity and thermodynamics in thunderclouds (X. Qie et al., 2020). Several studies have already been conducted using STORM973 data, including lightning data from the Beijing Broadband Lightning Network

(BLNET) and an operational S-band Doppler radar from the Beijing Meteorology Bureau (Chen et al., 2020; Lu, Qie, Jiang, et al., 2021; X. Qie et al., 2020; Sun et al., 2021; Xiao et al., 2021). BLNET is a 3D lightning detection network covering the whole metropolitan area of Beijing and parts of the Hebei Province (110 km east-west and 120 km north-south). BLNET consists of 16 stations able to geolocate both intra-cloud (IC) and CG lightning (Y. Wang et al., 2016) by using the time-of-arrival method. The average detection efficiency of BLNET is 93.2% for total lightning (Srivastava et al., 2017). Flashes are calculated from a flash-cluster algorithm screening and processing of the lightning sferics, that is, radio emission. Sferics within 400 ms and 15 km are grouped as one flash, and positive or negative CG is distinguished by whether the flash contains positive or negative return strikes (Lu, Qie, Jiang, et al., 2021; X. Qie et al., 2020).

A bilinear interpolation algorithm is adopted to transform the radar data into a regular Cartesian coordinate system with a horizontal resolution of 0.01° (latitude) \times 0.01° (longitude) and a vertical resolution of 0.5 km (H. Wang et al., 2009).

2.2. Introduction of *E*-WRF

The base code for the *E*-WRF module is developed and implemented into the WRF model (version 3.9.1.1; Skamarock & Klemp, 2007) by Fierro et al. (2013). Coupled with the NSSL 2-moment 4-ice microphysical scheme (Mansell et al., 2010; Mansell & Ziegler, 2013; Ziegler, 1985) and an explicit electrification and lightning parameterization, *E*-WRF is capable to simulate in-cloud electrical processes and lightning activities. A complete and detailed introduction to the charge separation, discharge algorithm, and the related equation solver for the electric potential is provided in Mansell et al. (2005, 2010) and Fierro et al. (2013). Compared with some existing diagnostic lightning prediction schemes, the CG lightning flashes simulated by the *E*-WRF model show better performances (Dafis et al., 2018).

The NSSL bulk microphysical scheme predicts the mixing ratios and number concentrations for six classes of hydrometeor: cloud droplets, raindrops, ice crystals, snow, graupel, and hail. Noninductive charging schemes in *E*-WRF account for the charge separation resulting from rebounding collisions between ice particles (riming graupel-hail and snow-ice) in the presence of supercooled cloud water without the need for the pre-existing ambient electric field. The noninductive charging schemes used here are based on Saunders and Peck (1998) and Brooks et al. (1997), as described in Mansell et al. (2005, 2010). The simulations also calculate inductive charging (Mansell et al., 2005 based on Ziegler et al., 1991), in which charge separation happens during rebounding collisions between cloud droplets and ice-phase particles (such as ice, graupel, and hail) in the presence of an electric field. Additionally, charge transfer during the mass exchange between hydrometeor species along with sedimentation and advection of space charge are all considered. The 3D electric field is explicitly solved through the computationally efficient MPI multigrid elliptic equation solver (BoxMG; Dendy, 1987). The discharge process uses a bulk approach based on the work of Ziegler and MacGorman (1994) and MacGorman et al. (2001). The initiation of a discharge depends on the breakdown critical threshold (E_{crit}), which can be constant (e.g., 120 kV m^{-1}) or height-dependent (Dwyer, 2003). The bulk discharge expands into a cylinder with a specific radius (usually set to 6–12 km) centered on the initiation point and vertically extending throughout the model column.

The *E*-WRF 2D lightning output field “LIGHT” is the sum of lightning initiations in the cylinder column and can be calculated to estimate the flash origin density. The output from *E*-WRF also includes predicted 3D electrical parameters such as the electric potential, the x -component, y -component, and z -component of the electric field magnitude, the net noninductive/inductive charge separation rate, and the charge density carried by the six hydrometeor types considered in the NSSL scheme.

2.3. Simulation Setup

Figure 1 shows a map of the triple-nested WRF simulation domain used herein, with the innermost domain (d03) specifically designed to cover the whole metropolitan area of Beijing, Tianjin, and most of the Hebei province. Table 1 provides a summary of the basic WRF settings. The simulation started on 20150727 0000 UTC and ended at 1800 UTC. The NCEP FNL global operational analysis data set with a horizontal resolution of $1^\circ \times 1^\circ$ is employed to derive the initial and boundary conditions for the simulations.

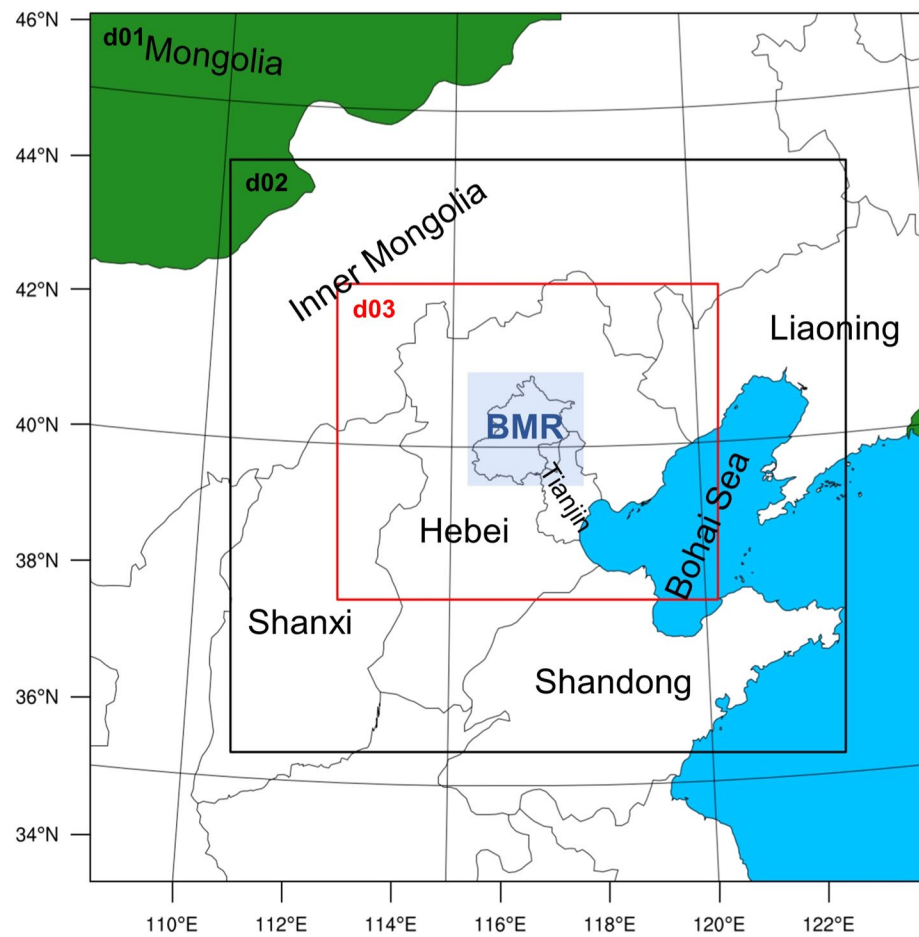


Figure 1. Map of the triple-nested Weather Research and Forecasting simulation domain.

Table 1
The Basic Configuration of the WRF Model and Its Physical Parameterizations

Parameter	Property
Horizontal resolution	4.5 km, 1.5 km, 0.5 km
Number of vertical levels	34
Model top	50 hPa
Time steps	18 s
Simulation duration	18 hr
Number of grids points	310 × 310, 688 × 634, 1,276 × 1,012
Boundary layer scheme	BouLac
Longwave radiation scheme	RRTM
Shortwave radiation scheme	Dudhia
Microphysics scheme	NSSL 2-moment 4-ice
Cumulus parameterization scheme	None
Surface layer scheme	RMM5
Land surface scheme	Noah

Electrification is activated in d03 only. The settings are similar to the previous simulations (Dafis et al., 2018; Fierro et al., 2013; Sun et al., 2021). In this simulation, the background cloud condensation nuclei concentration is set to a higher value of $0.8 \times 10^9 \text{ m}^{-3}$, considering the pollution of Beijing (Sun et al., 2021). Both inductive and noninductive charging processes are considered, in which the noninductive rime accretion rate (RAR) scheme has been improved by Mansell et al. (2010). The height-dependent breakdown electric field profile of Dwyer (2003) is used. The discharge cylinder radius is set to 6 km and 30% of the charge is removed per discharge within the cylinders (Fierro et al., 2013).

2.4. Identification of the CM

In this study, a cell (or larger, a storm) is identified as an area bounded by 30 dBZ composite reflectivity, with one (or quasi-continuous) very compact strong echo core (Gauthier et al., 2010; Lu, Qie, Jiang, et al., 2021; Westcott, 1994). The contact of the 30 dBZ boundary between two isolated cells or storms is considered the start of the CM, and the coalescence of the strongest echo cores (which is higher than 45 dBZ in this case) as the end of the CM.

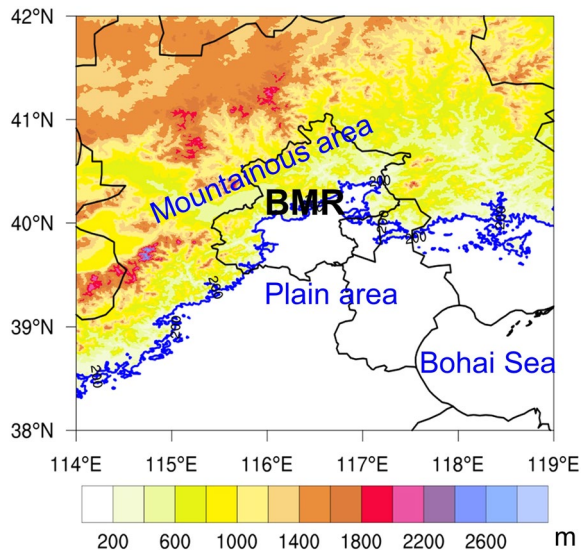


Figure 2. Surface elevation (m) around the Beijing Metropolitan Region (BMR). The 200 m indicated by the blue thick contour line was the dividing line of plain and mountainous areas.

3. Case Overview

As shown in Figure 2, the BMR area is characterized by mountainous in the north, northwest, and northeast, and plain in the southeast, and about 100 km from the sea to the east. Coupled with densely populated urban areas, it forms a complex underlying surface, which can affect the initiation and intensification of convections through topographic uplift and urban heat effect.

Based on a 5-year observational study from 2014 to 2018, the squall line is one of the most common severe weather system types over the BMR (X. Qie et al., 2020). And the squall line on July 27, 2015 was one of the most severe thunderstorm cases that occurred during the STORM973 campaign. At 500 hPa, The BMR is affected by the two deep cold vortexes (northeast cold vortex near 125°E and Mongolia cold vortex near 100°E) and subtropical high (Figure 3a). The upstream Mongolia cold vortex moves fast to the east and constantly gets close to the northeast cold vortex, both bringing cold air in the northwest. And the subtropical high brings warm and humid airflow from the southwest, forming a wet tongue with specific humidity greater than 70%, extending along Taihang Mountain. Moreover, a shear line formed in northwest of the BMR. The Beijing radiosonde at 1400 LST (= UTC + 8 hr) showed a surface water vapor mass mixing ratio exceeding 20 g kg^{-1} . The convective available potential energy was over $3,400 \text{ J kg}^{-1}$, and the convective inhibition was marginal below -20 J kg^{-1} (figure not shown). Consequently, the pre-storm environment on that day was particularly favorable for the initiation of deep mixed-phase and electrified convection.

Figure 4 shows the composite reflectivity evolution of the squall line system. Multiple isolated cells were initiated before 0700 UTC over the northwest mountainous region of the BMR (figures not shown), then propagated southeastward toward the BMR plain area under the background westerly wind. They strengthened and expanded after a series of mergers with small meso β and γ scale cells.

At 1100 UTC (Figure 4a), they formed into two main linear storms longer than 150 km labeled B and C0, with three smaller cells C1, C2, and C3 in front of storm C0. These storms propagated and gradually got closer to each other. The storms B and C0 were linked through a few small and dense newborn cells between storms B and C, and the small cells C1, C2, and C3 were also integrated into storm C0 (labeled C, Figure 4b), hence they started to grow upscale into a longer complex storm. Based on the CM criteria defined above, it is the beginning of the

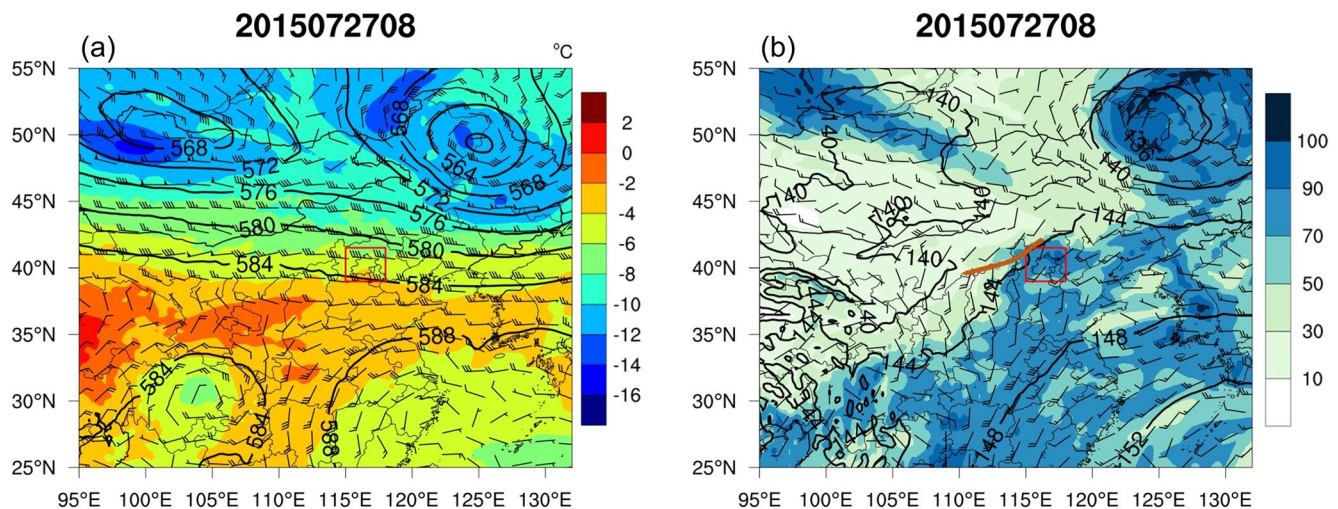


Figure 3. (a) The 500 hPa geopotential height (black lines, dagpm) and temperature (shaded, °C), and (b) the 850 hPa geopotential height (black lines, dagpm), specific humidity (shaded, g/kg), and wind barb (m/s) at 0800 UTC on July 27, 2015. The red dashed box represents the Beijing area. The wind shear line is marked by a brown segment. (Reanalysis data from ERA-5, ECMWF.)

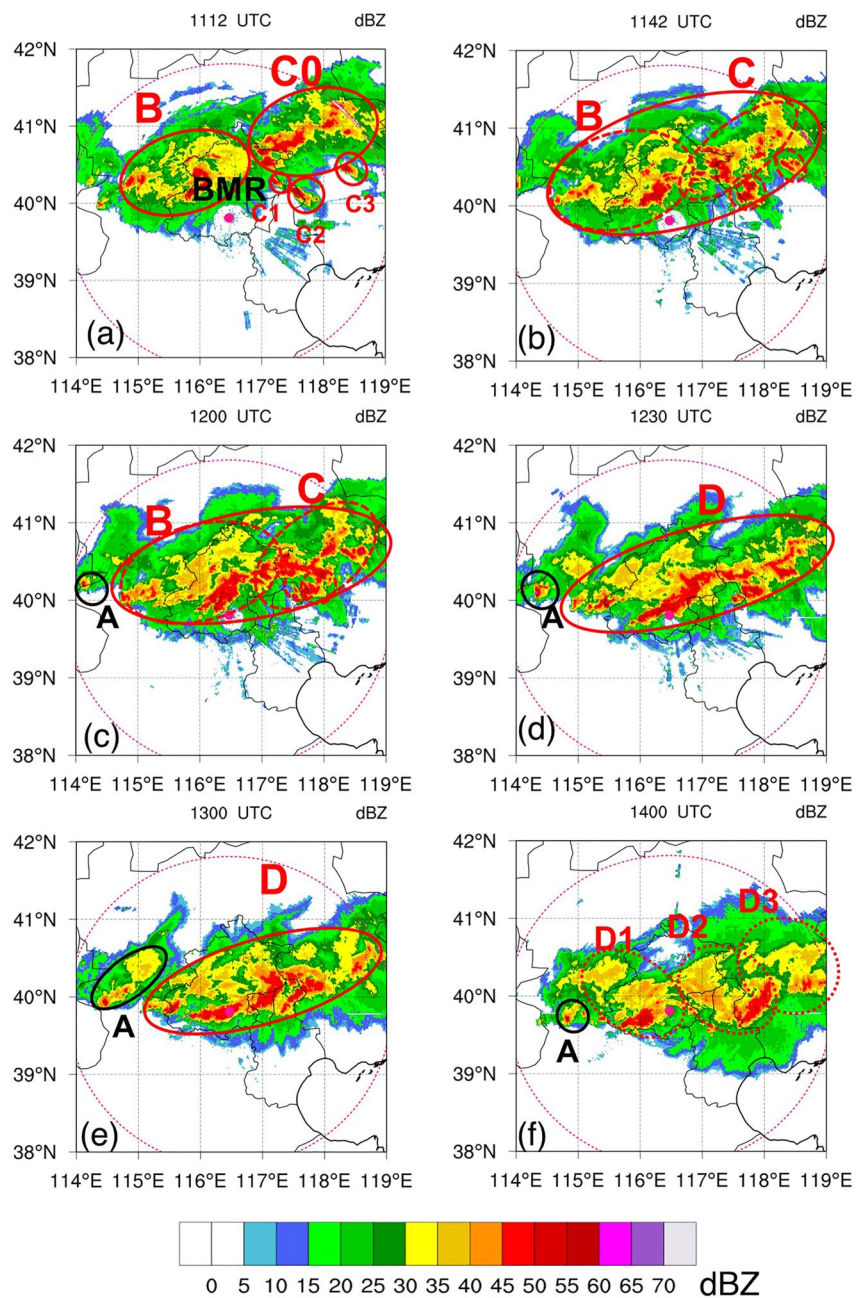


Figure 4. Composite reflectivity (color-shaded) was observed by the S-band Doppler radar (site location is marked with a pink dot) on July 27, 2015. The radar's effective detection radius was about 230 km (pink dashed circle). The main convective storms are labeled (A)–(D), respectively. The cells and storms involved in the squall line are marked by red circles. The convective merger period between storms B and C was 1142–1230 UTC.

CM (1142 UTC). In Figure 4c, there was a small cell (labeled A) that existed in the west of the main system, with a stable distance of about 30 km. The main storms kept merging, until 1230 UTC (Figure 4d), and the strong echo core was the most compact and was regarded as the end of the CM by definition. The mature structure of the squall line (labeled D) formed at this moment, with a length longer than 250 km. During the CM, lightning activity dramatically increased more than threefold within about 1 hr, from about 400 fl (6 min)⁻¹ to about 1,400 fl (6 min)⁻¹ (described in detail in the following Section 4). The mature stage was sustained for more than 1 hr (Figure 4e), during which the precipitation rate exceeded 40 mm hr⁻¹ and was accompanied by strong gusts exceeding 14 m s⁻¹, and hail (X. Qie et al., 2020). Then the squall line gradually weakened and split into three

separate storms labeled D1, D2, and D3 (at 1400 UTC, Figure 4f), then quickly moved beyond the BMR area. This weather storm completely dissipated around 1700 UTC, and the total life cycle was about 10 hr.

4. Validation of the Model Simulations

Model verification and comparison based on the observational radar reflectivity and lightning flash data rate are conducted in this section. Figure 5 shows the composite reflectivity simulated by *E*-WRF. The general simulation evolution lagged the observation by about 48 min (Figures 5a–5e), but the decay stage in Figure 5f is 1 hr and 36 min later than the observation (Figure 4f).

In general, the observed main storms B, C, and the formed squall line D aforementioned are successfully captured in the *E*-WRF simulation. And the key CM process between storms B and C compare quite well in time and space to the observations, which is the basis for later analysis. Also, cell A propagated slowly and did not participate in any merging with other storms in the simulation, which is consistent with the observation (Figures 4a–4e); however, the distance between cell A and the main storm, and the size of cell A are overestimated to some extent compared with reality.

The CM process is shown in Figures 5b–5d. The 30 dBZ boundaries of storms B and C connected at about 1230 UTC (Figure 4b, as the start of the CM) and the 45 dBZ cores merged at 1318 UTC (Figure 5d, as the end of the CM), both lagged the observations by 48 min. The horizontal scale of the main body of squall line D is about 230 km (Figures 5d and 5e), which is comparable to that of the observed squall line (about 250 km). The squall line becomes weak around 1536 UTC (Figure 5f). Even though the simulated life cycle lagged a few minutes, and the storms are shifted by about 80 km far to the east, the characteristics of storm evolution and storm merging processes can be regarded as well reproduced.

Figure 6 shows the spatial distribution of observed and simulated lightning activities. The majority of observed flashes are IC flashes, and all types of flashes are mainly distributed in the strong echo area within the convective line, some flashes are distributed just behind the convective line, and only a few occurred within the trailing stratiform area. The lightning activity in storm B is more vigorous than in storm C in both observation and simulation. It is speculated that the reason may be that the trajectory of storm B is closer to the center of the BMR, so it is affected by the stronger heat island effect. The observation results show that after the CM (since 1142 UTC, Figure 6a), the lightning surged near the region between the old storms (called cloud bridge region R), and even exceeded that of storm B (1230 UTC, Figure 6e). In the corresponding period of the simulation (1230–1318 UTC, Figure 6f), there also generated a new lightning center, but the amplification is not as much as observed.

Figure 7 shows the normalized lightning flash (by maximum value) variation of observation and simulation. Here we take the normalized lightning to avoid focusing on differences in flash rates between the observations and simulations because of some reasons (e.g., the group algorithm in the observation, and discharge settings such as discharge ratio and radius). The observed thunderstorm complex entered the effective detection coverage of the BLNET at around 1000 UTC. The normalized total lightning flash rate simulated by *E*-WRF is quite consistent with the observations, especially after 1130 UTC. The lightning rates both rapidly increase in 18–24 min after the beginning of the CM and peak at this stage, followed by a sharp decline starting at 1300 UTC of observation and 1348 UTC of simulation (the lightning decline is much earlier than that of composite reflectivity, see in Figures 4e and 4f and Figures 5e and 5f). In general, the simulated lightning activity compares quite well in time and space to the observations, which are deemed suitable to conduct further in-depth analysis.

5. Results

5.1. Storm-Scale Lightning Activity

Figure 8 shows the stacked histogram of the simulated lightning flash frequency for main storms B, C, and D near the CM period. The sum of lightning flash frequency in B and C, or D accounts for over 95% of the total flash frequency of the squall line. The lightning activity associated with storm B is more pronounced and accounted for over 75% of the pre-CM flash total. At 1206 UTC (24 min before the CM), the flash frequency of both B and C decreases, with values reaching a minimum below 10 fl (6 min)⁻¹. The lightning frequency surges by more than 2.5 fold during the first 18 min following the beginning of the CM to reach peak values exceeding 30 fl (6 min)⁻¹

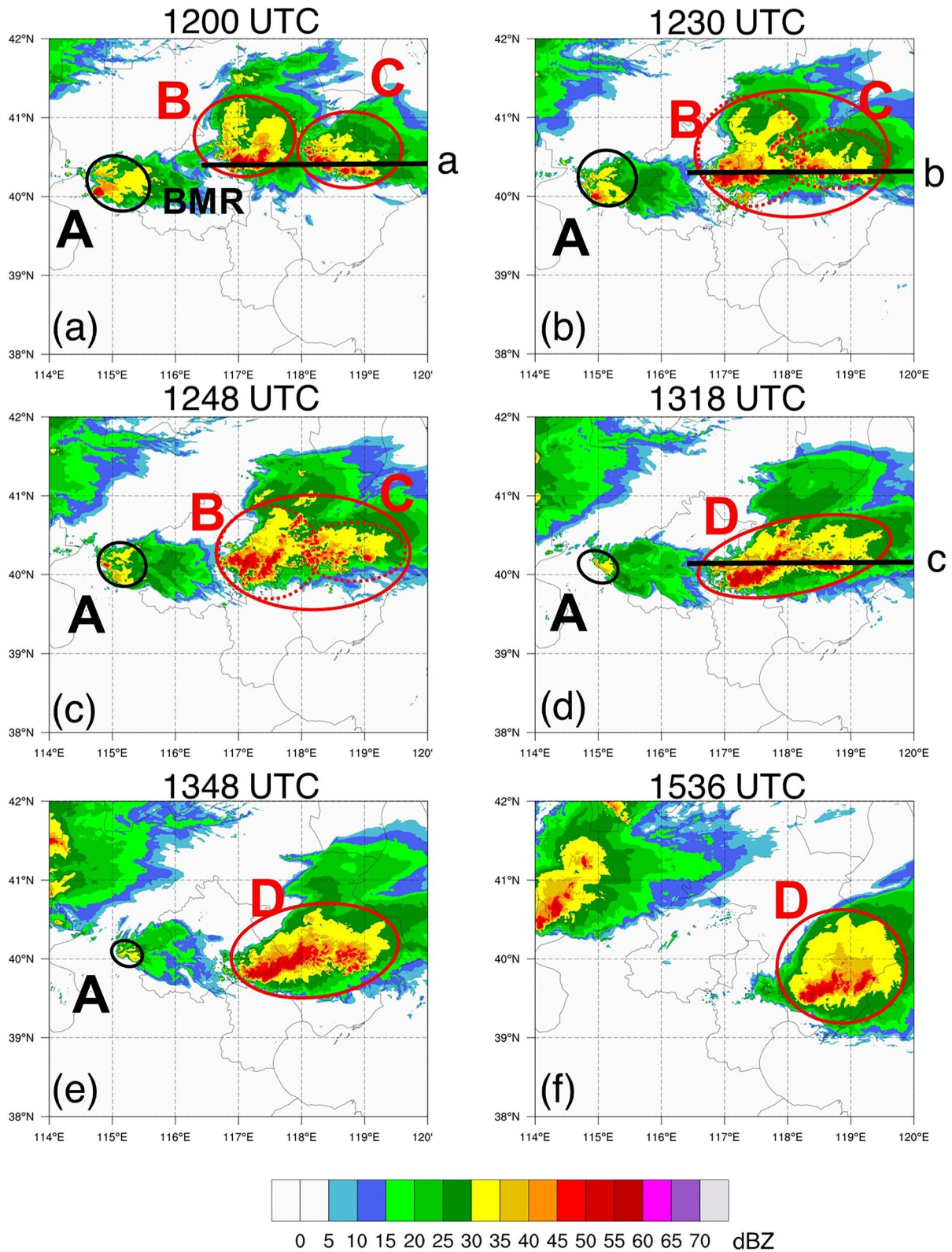


Figure 5. Composite reflectivity (color-shaded) simulated by E-WRF (all simulation-times are observation-times+48 min, compared to Figure 4). The cells and storms involved in the squall line are marked by red circles. The convective merger (CM) period is 1230–1318 UTC. The black lines labeled (a)–(c) in (d)–(f) are the section lines along the leading convective line for Figures 10 and 12.

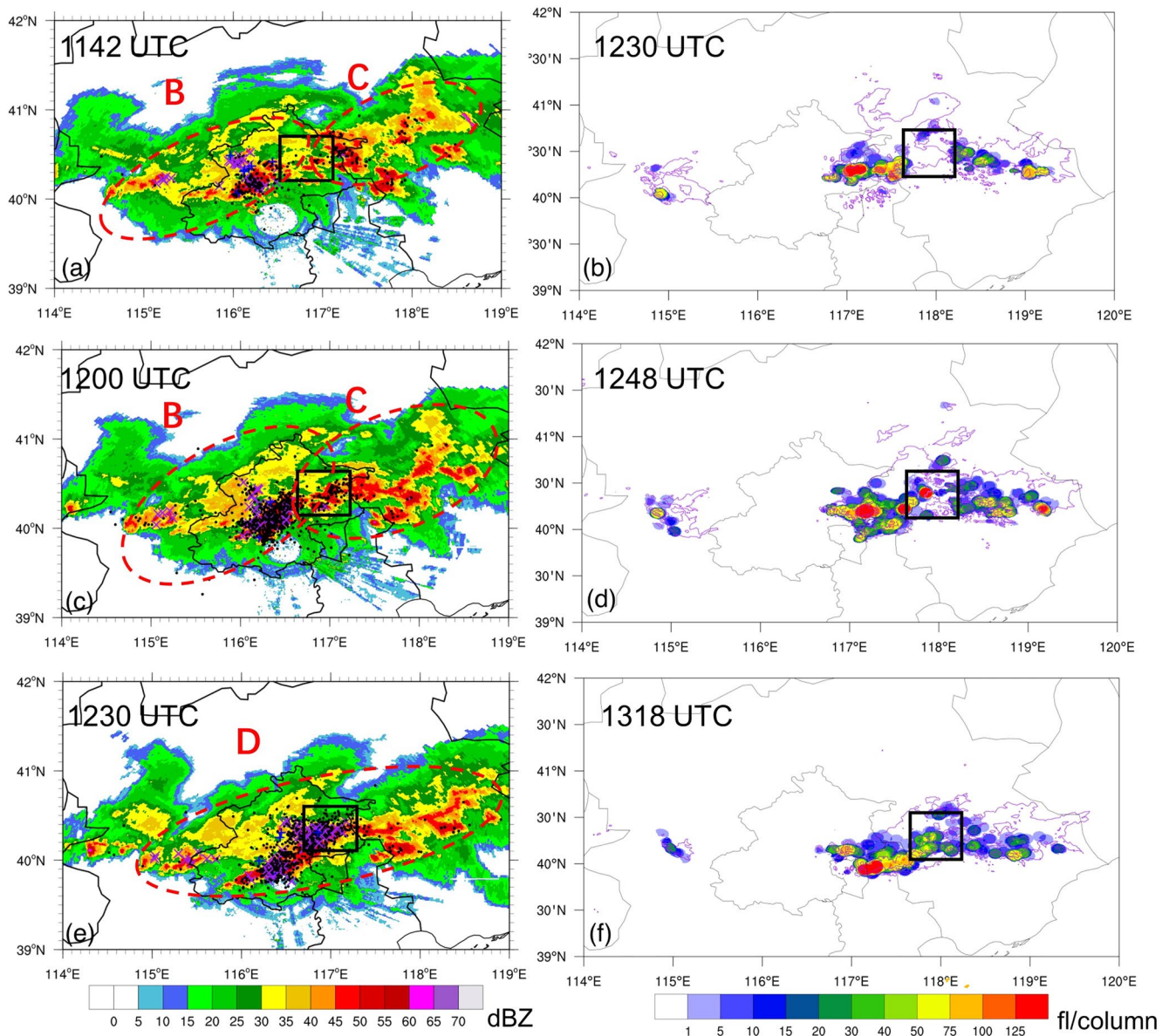


Figure 6. Left column (a, c, e): Observed composite reflectivity (left column: shaded) and corresponding 6-min lightning flashes detected by BLNET. Right column (b, d, f): Simulated composite reflectivity (purple contour lines indicate 30, 40, and 50 dBZ) and corresponding 6-min simulated flash extent density by E-WRF. (a, b) are the beginning of the convective merger (CM), (c, d) are the middle of the CM, (e, f) are the end of the CM. The black square represents the selected region (R) near the cloud bridge. Flash extent density is the sum of the number of flashes that extend into the grid column (with radius of 6 km).

at 1248 UTC. The very active lightning lasts about 1 hr and 18 min, then drops back to the pre-merger level of $20 \text{ fl (6 min)}^{-1}$ at 1348 UTC.

5.2. Thermodynamics of CM Process

Figure 9 shows the integrated updraft (i.e., w) volume of the whole system. After the CM, the volumes of $w > 5 \text{ m s}^{-1}$ at 5–9 km (centered at 6 km, the ambient temperature altitude information can be found in Table 2) and $w > 2 \text{ m s}^{-1}$ at 4–11 km (centered at 8 km) both increase significantly. However, the $w > 5 \text{ m s}^{-1}$ at the upper level (8–11 km) is larger around 1000 and 1100 UTC, which also produces lightning flashes (see Figure 7). The updraft zones are in different cells which are weakly organized during this time, so the lightning flashes are weaker than during the CM period. The high-level updraft at 9–12 km becomes weaker after the CM, and the

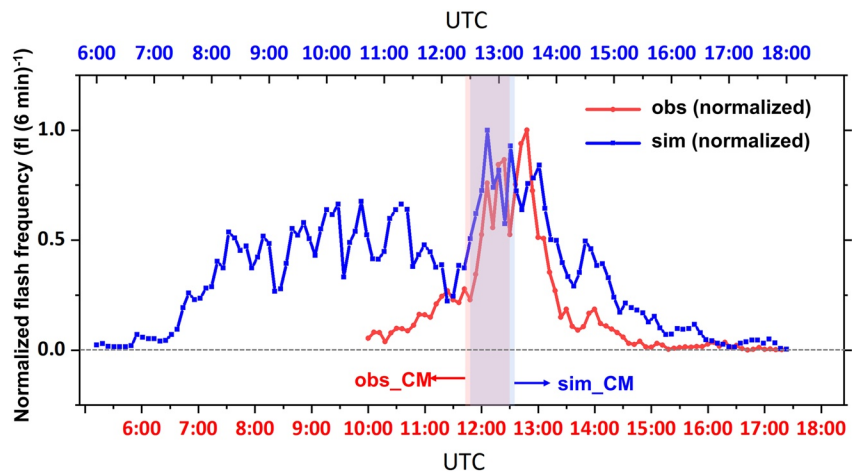


Figure 7. Temporal variation of the observed (red, corresponding to the bottom red time label) and E-WRF-simulated (blue, corresponding to the top blue time label) normalized total lightning flash frequency. The two time axes have a 48-min difference. The red and blue block marks the observational and simulated convective merger (CM) period.

strong updraft is more concentrated in the 0–20°C layer. The later Section 5.3 analyzes more details linking to microphysical processes. The $w > 2 \text{ m s}^{-1}$ contours over 18 km height before the CM is partially attributed to the numerical artifact.

Figure 10 shows a more detailed thermodynamic field around the CM period. The maximum updraft speed of storm B exceeds 27 m s^{-1} prior to the CM, and the intense precipitation produces a thick (about 1.5 km) and wide (about 40 km) cold pool. After the onset of the CM (Figure 10b), the updraft of storms B and C weakens, and the 30 dBZ echo top of storm B decreases from 14 to 12 km. However, a new updraft center forms near 118°E at 4–8 km and then produces new cells. The cloud bridge is established both through the upper-level anvils and mid-level new cells. After the CM (Figure 10c), the new precipitation of the cloud bridge and its evaporation connected the old cold pools, forming a very wide (at least 150 km) surface cold pool with an intensity of exceeded -3.5K . The extended cold pool dynamics lead to stronger near-surface convergence between storms, and, ultimately 30 m s^{-1} updraft which is conducive to the growth of new cells.

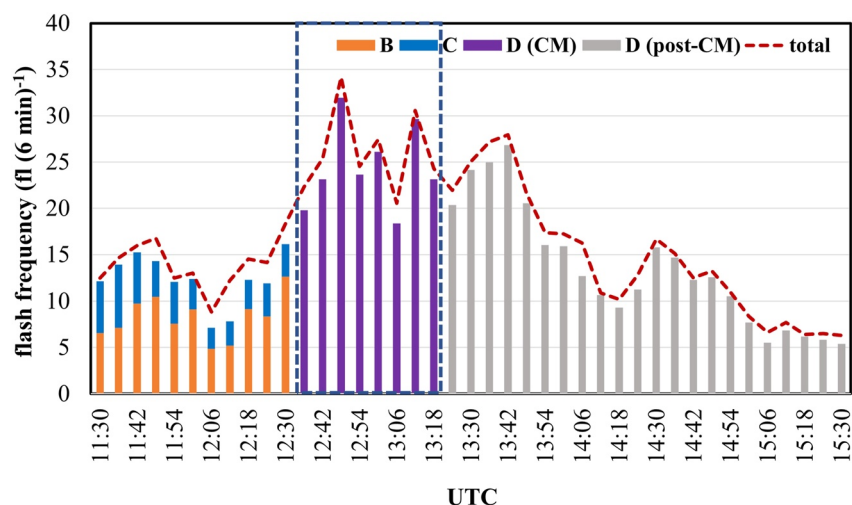


Figure 8. Stacked histogram of the lightning flash frequency simulated by E-WRF for systems B, C, D, and total flash frequency of the whole system (dashed dark red line) around the convective merger (CM) period (dashed vertical blue lines).

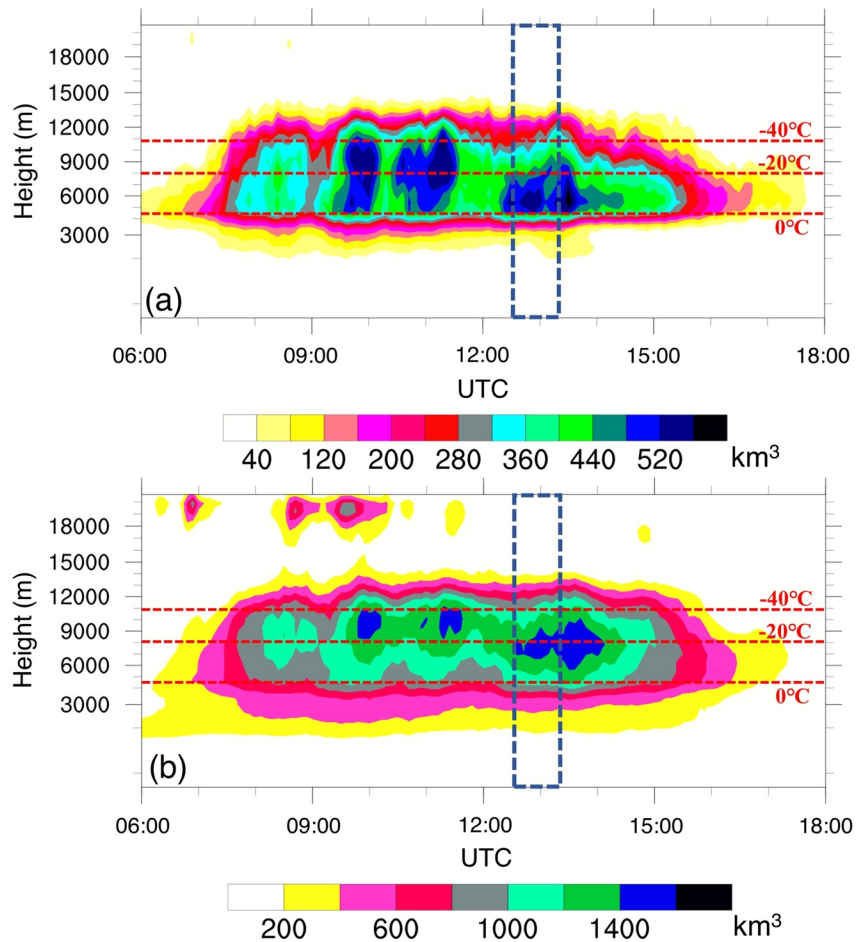


Figure 9. Variation of the integrated volume of (a) $w > 5 \text{ m s}^{-1}$, and (b) $w > 2 \text{ m s}^{-1}$ of the whole squall line (color-shaded, units: km^3) from 0600 to 1800 UTC. It is calculated by the sum of the volumes of all grid that $w > 5 \text{ m s}^{-1}$ or $w > 2 \text{ m s}^{-1}$, and $\text{Volume}_{\text{grid}} = \Delta A \times \Delta h$ (where the ΔA is $500 \times 500 \text{ m}^2$; Δh is the specific vertical resolution of this layer). The red dashed lines are the ambient isotherms of 0°C , -20°C , and -40°C . The blue dashed lines indicated the convective merger period.

5.3. Electrical and Microphysical Characteristics

Figure 11 shows the vertical and temporal distribution of the storm-integrated net space charge. During the early, isolated multiple cell stage, the net space charge presents a normal tripolar (“Positive-Negative-Positive,” hereinafter referred to as “P-N-P”) vertical structure. The lower P charge layer is located mainly at 1–4 km (AGL, all the same below), the N charge layer is a thicker layer mainly located at 5–12 km, and the upper P charge layer dominates primarily at 11–13 km.

When storms B and C weaken just prior to merging, the charge structure exhibits more distinct features: the average height of the upper P charge layer drops down to about 10 km while the main midlevel N charge layer becomes thinner. The lower P charge layer begins to dissipate before 1000 UTC then the original normal tripolar P-N-P charge structure shifts into a temporary inverted bipolar N-P vertical charge structure characterized by overall weaker charge magnitudes, which corresponds to the decrease in lightning activity from 1030 to 1130 UTC (refer to Figure 7).

Before 1200 UTC, the positive and negative charge tended to be a more mixed structure and they both expanded to all levels at 0–13 km. When the CM begins (1230 UTC), a more clear five-layer (P-N-P-N-P) charge structure forms, including three P charge layers near 5 km, 10 km, and 13 km, and two N charge layers centered near 7 km (already existing and its center shifts upward about 1 km), and 12 km. This five-layer (P-N-P-N-P) charge structure is basically caused by the charge of the convection region (see Figure 12 below for details), and it is

Table 2
The Temperature (From -60°C to 20°C) Altitude of the Squall Line

Height (km)	Temperature ($^{\circ}\text{C}$)
2.1	20
2.9	15
3.9	10
4.6	5
5.4	0
6.2	-5
7.0	-10
7.8	-15
8.5	-20
9.3	-25
10.1	-30
10.9	-35
11.6	-40
12.4	-45
13.2	-50
13.9	-55
15.5	-60

similar to that previously reported by Stolzenburg et al. (1998). Interesting, five-layer pockets already occur before CM (at 1200 UTC) in many segments of regions B and C (approximately 117.25° – 117.5°E and 118° – 118.5°E). We speculate that some physical processes (including the mixtures of elevated weak updrafts and downdrafts near 6–9 km) during CM may extend these pre-existing subregions throughout the line.

Figure 12 shows the net charge density of the leading-convective line (Figures 12a–12c), the vertical profile of vertical electric fields (E_z) of storms B and C, and the cloud bridge (Figures 12d–12f) around the CM period. During this time, the charge structure gradually evolves from staggered smaller charge pockets to a vertically stratified five-layer structure, with larger net charge density values. The maximum absolute value of net charge density in the squall line is about 0.65 nC m^{-3} at 1200 and 1230 UTC, and then increases 2.5 times to about 1.6 nC m^{-3} at 1318 UTC. After the CM, the vertical five-layer charge structure forms. The wider charge regions, more dense charge, and the reduction of spacing between the layers lead to a dramatic increase in the E_z , especially at the cloud bridge, where it increases more than threefold, and ultimately results in a dramatic increase of lightning initiations.

Figure 13 shows the storm-integrated charge and mass of graupel, snow, and cloud ice, which made the most important contributions (>80%) to the net space charge among the six hydrometeor types. The contribution from the other three hydrometeor species (cloud water, hail, and rain) to the total net charge are relatively smaller and not shown.

The storm-integrated mass of graupel is relatively low, with the peak exceeding 30 kg near 7 km. After the onset of the CM, the graupel is more concentrated vertically, probably due to the stronger mid-level (5–10 km, Figures 9 and 10) updrafts and weaker upper-level (>11 km) updrafts. From the Mansell et al. (2010, based on Saunders & Peck, 1998; Brooks et al., 1997) charging curve, graupel charges positively within regions of relatively strong updrafts (Figures 9 and 10) and larger RAR at lower levels (6–7 km, 0°C to -20°C , Figure 13), and charged negatively at higher altitudes (9 km, -20°C to -40°C), where temperatures and RAR were lower. During and after the CM, the graupel mass and positive charge both increase, contributing to the lowest P charge near 5 km (Figure 11).

After the onset of the CM, the storm-integrated snow mass and the charge of snow both increase dramatically, with a maximum exceeding 50 kg at 8–10 km, carrying a positive charge of more than $20 \mu\text{C}$. It is worth noting that, the intensified $w > 2 \text{ m s}^{-1}$ and $w > 5 \text{ m s}^{-1}$ (Figure 9) are similar to the increased layer of mid-level snow and graupel mass, respectively. After the CM, the increase of mid-level snow (near 6 km) and graupel mass (near 8 km) correspond to the increase significantly in volumes of $w > 5 \text{ m s}^{-1}$ at 5–9 km (centered at 6 km) and $w > 2 \text{ m s}^{-1}$ at 5–10 km (centered at 8 km), respectively (Figure 9).

Cloud ice is lighter so distributes higher than any other hydrometeors, with a peak value of storm-integrated mass exceeding 40 kg at 12 km. The reduction of cloud ice mass at the upper level after the CM is also consistent with overall weaker high-level updrafts (9–12 km) in Figure 9. The final charge layers seem to be effectively influenced by sedimentation and advection of space charge, especially on a small mixing ratio, then resulting in a stable thin-upper-P and thick-lower-N charge centered at 13 and 6 km, respectively.

Here we analyzed the specific contributions of graupel, snow, and cloud ice (Figure 13) in forming a five-layer net space charge (Figure 11). The evolution of graupel storm-integrated mass influences the lowest P charge region. Prior to the CM, the storm-integrated graupel mass decreases, leading to the weakening of the lowest P charge layer and causing the decrease in lightning activity after 1100 UTC (refer to Figure 7). After the onset of the CM, the increases in the storm-integrated mass of graupel, raindrops, and hail (not shown) reinvigorates the lowest P charge layer. Meanwhile, both cloud ice and snow are chief contributors to the mid-lower N charge layer near 7 km. The middle P charge layer near 10 km is almost completely associated with snow while the mid-upper N

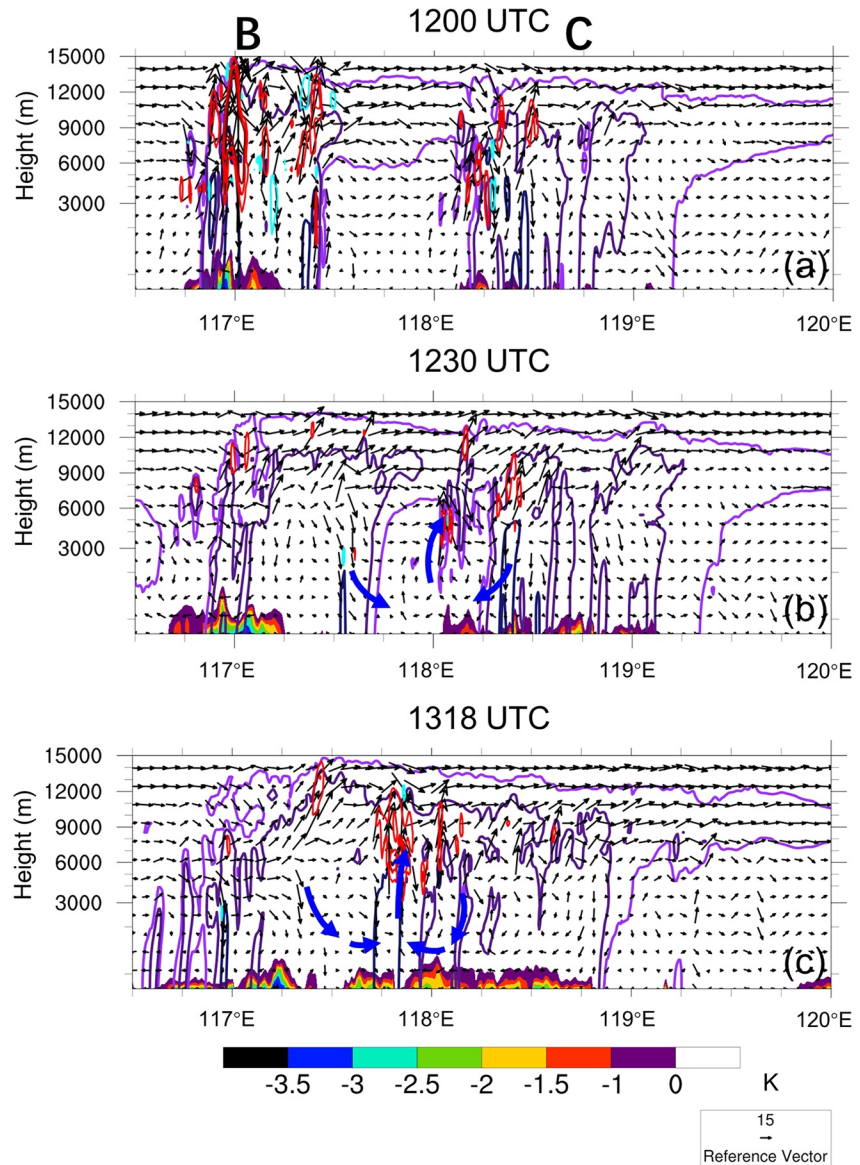


Figure 10. Thermodynamic field of the convective line along (a)–(c) in Figure 5, (a) before the convective merger (CM), (b) at beginning of the CM, and (c) at end of the CM. Updraft 5, 10, and 15 m s^{-1} are in red lines; downdraft -5 m s^{-1} in blue lines; 10, 30, and 50 dBZ radar echo in the purple line, and perturbation potential temperature in color-shaded (area $<0\text{K}$ considered as the cold pool). Blue arrows indicate circulation.

charge layer near 12 km is primarily attributed to cloud ice, with a comparatively smaller fraction from graupel (7%). The uppermost P charge layer near 14 km is almost exclusively attributed to cloud ice, with only a small fraction (4%) associated with snow and graupel.

5.4. Ice Particle Budgets

The budget equation of the mixing ratio is applied to analyze the changes in three hydrometeor types (cloud ice, snow, and graupel, abbreviated as q_{ice} , q_{snow} , and q_{graupel} , and uniformly expressed as q_i herein) near the cloud bridge region (labeled R, where seems to be the most obvious changing area). The q_i budget Equation 1 includes the tendency term, horizontal advection term, vertical transport term, and residual term:

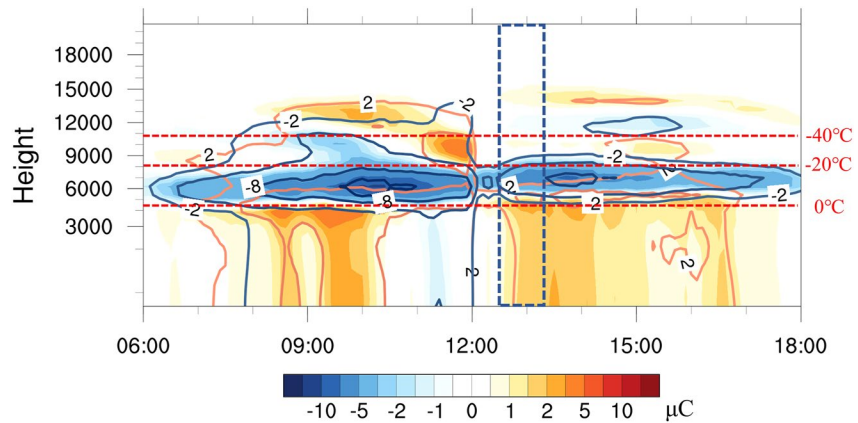


Figure 11. Variation of integrated positive (red contour lines, from 2 to 8 μC), negative (blue contour lines, from 2 to 8 μC), and net space charge of the squall line (color-shaded, units: μC) from 0600 to 1800 UTC. The red dashed lines are the ambient isotherms of 0°C, -20°C, and -40°C. The blue dashed lines indicated the convective merger period.

$$\frac{\partial q_i}{\partial t} = -\vec{V}_h \cdot \nabla q_i - w \frac{\partial q_i}{\partial z} + F_y \quad (1)$$

where q_i is the mixing ratio at a level z probably of a specific zone, and the w and \vec{V}_h are the vertical and horizontal components of velocity. The residual term F_y includes microphysical source and sink terms (e.g., freezing, melting, condensation, and evaporation), turbulent diffusion, and computational errors.

Figure 14 shows the vertical/horizontal transport of specific ice-phase particles at their most concentrated level. Overall, CM plays a very important role in the local growth for graupel: there is no significant increase in graupel before the onset of the CM. During the CM, the graupel mass mixing ratio increases dramatically, during which time the horizontal transport, vertical transport, and residual terms all contribute at various levels. Horizontal transport is dominant at first, which indicates that the midlevel transport carries the graupel toward the cloud bridge region (R). After that, the vertical transport increases rapidly to exceed the effect of horizontal transport, which indicates that surrounding graupel particles are forming and growing, and are lofted by stronger vertical motions. The residual term provides a positive contribution at the beginning of CM, and then plays a largely negative role, which may be due to the conversion to other types of hydrometeors.

During the CM, the local variation of snow is basically weakly negative except near the end of the CM. After the CM begins, however, the vertical transport of snow becomes dominant, and the newly generated snow in the lower layer is transported to the upper layer by strengthening vertical motions. The contribution of the horizontal transport is relatively small.

Cloud ice shows significantly different characteristics. During the CM, the value of the local variation decreases by 1 order of magnitude. Vertical transport is also very small. The horizontal transport is more dominant than other terms.

In summary, the transport is very important in the cloud bridge area during the CM. The graupel near the cloud bridge (nearly at 7 km) increases due to the vertical transport corresponding to the strong updraft (see them in Figures 9 and 10). At the high layer of the cloud bridge, both snow and cloud ice have less local growth (weak tendency term). We inferred that the strong mid-level updrafts between 6 and 9 km (Figures 9 and 10) may bring existing particles outside of the cloud bridge.

6. Conclusion and Discussion

A severe squall line resulting from the mergers of several incipient isolated thunderstorm cells and storms is simulated and studied using an explicit cloud electrification scheme E -WRF. Qualitative validation of the simulation in terms of radar reflectivity and normalized flash frequency indicated that the model is able to reasonably

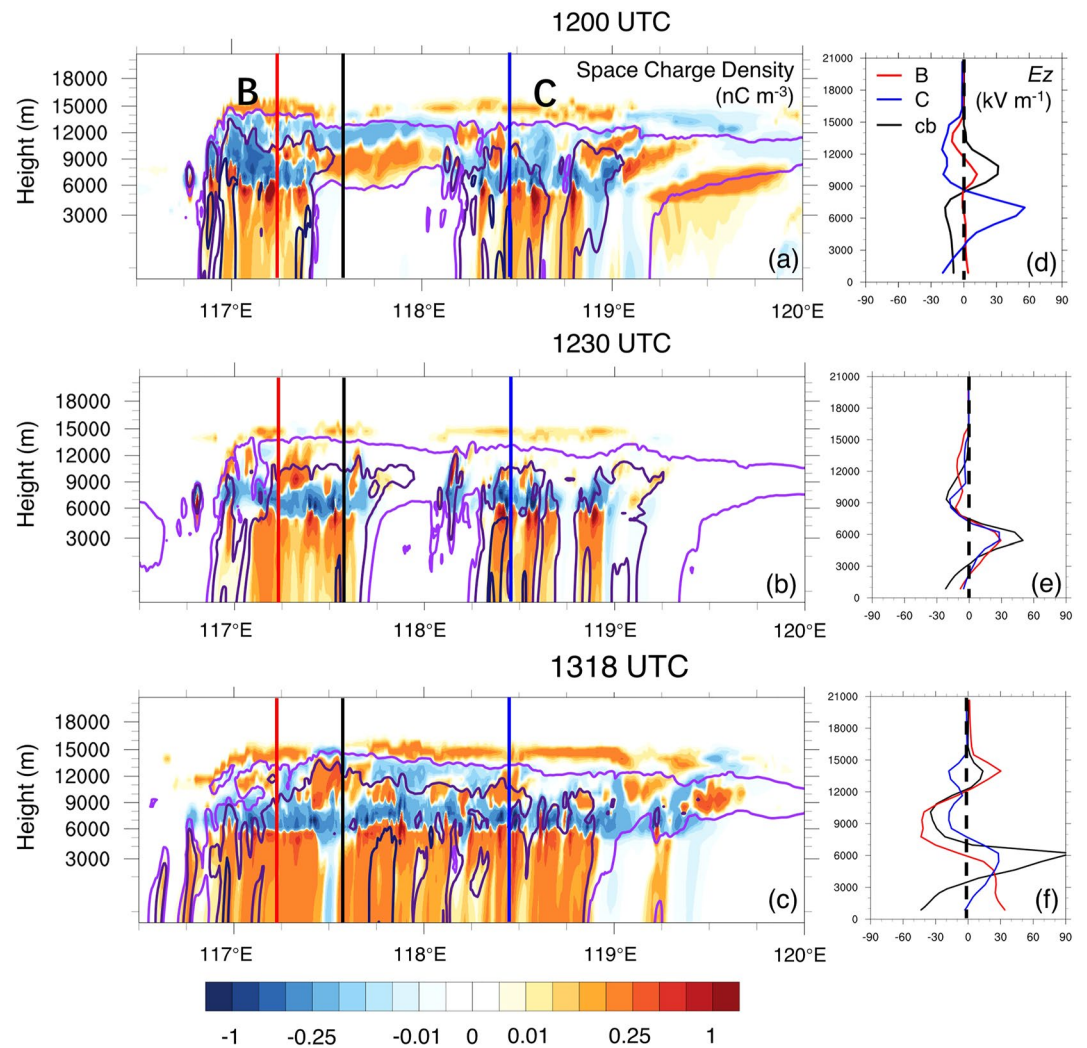


Figure 12. The charge density of convective line along (a)–(c) in Figure 5, (a) before convective merger (CM), (b) at beginning of the CM, and (c) at end of the CM; the deep purple contour lines represent radar echo of 10, 30, 50 dBZ. (d)–(f) Correspond vertical profile of vertical electric fields (E_z) along the section lines of storm B (red section line and curve), cloud bridge (cb, black section line and curve), and storm C (blue section line and curve).

reproduce the thunderstorm complex and associated lightning activity, as well as the critical merger processes of the main individual cells and storms.

The simulated CM processes and the CM-driven lightning surge are generally consistent with the observations. The associated charge structure involves redistribution from a staggered charge pocket structure into a vertically stratified five-layer charge structure from near-surface to 15 km. The wider charge regions, more dense charge, and the reduction of spacing of different charge layers significantly increase the vertical electric field magnitude, which is a causative factor of the lightning surge.

The microphysical mechanism of the lightning surge is examined through budget analysis of ice-phase particles. The increase in middle-layer snow and lower-layer graupel near the cloud bridge is facilitated by both the vertical transport of newly formed particles and the horizontal transport from upstream. The cloud bridge is produced by the upstream anvil propagation downstream, and the budget analysis reveals that the horizontal transport is the primary source of high-level cloud ice mass. The increasing ice-phase particles in the middle and downstream regions strengthen the collision rate, therefore, enhancing the noninductive electrification. Convergence between two merging storms in the middle and lower layers results in the formation of a new but stronger updraft center as the CM progresses. Then the cold pool expands and the new cells near the cloud bridge grow fast.

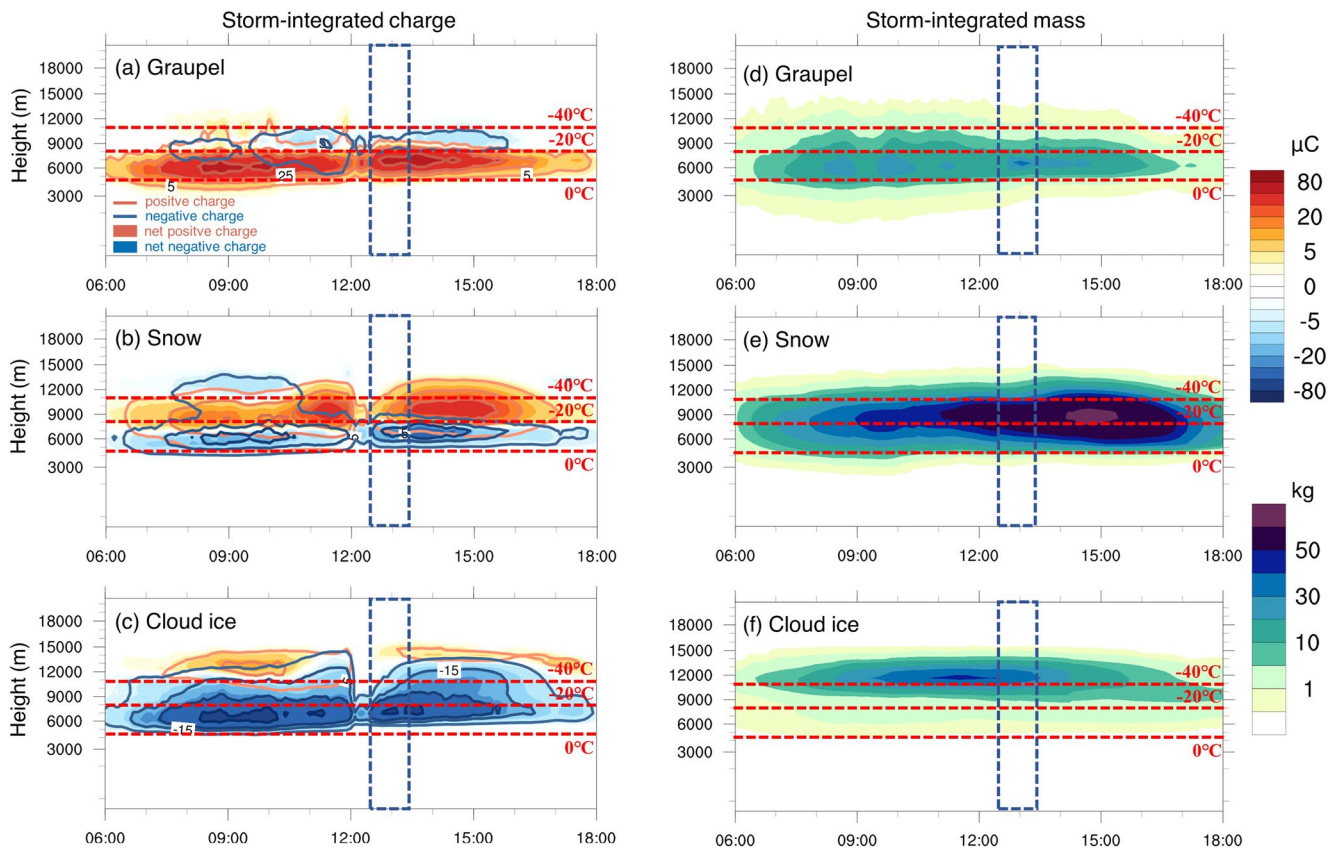


Figure 13. Same as in Figure 11 but, in the left column (a)–(c) are the storm-integrated positive (red contour lines, 5–50 μC with spacing of 15 μC), negative (blue contour lines, -50 to -5 μC with spacing of 15 μC), and net charge (color-shaded, units: μC) of (a) graupel, (b) snow, and (c) cloud ice; in the right column (d)–(f), storm-integrated mass (color-shaded, units: kg) of (d) graupel, (e) snow, and (f) cloud ice.

Figure 15 summarizes the pre-CM and post-CM dynamics, microphysics and charge features based on this work and highlights the unique role of CM from significant enhancement near the cloud bridge. Before merging, the two main incipient storms have their own distinct echo and updraft centers and initially came into contact via upper-level anvil downstream transportation of ice. After merging, a single, stronger reflectivity core and updraft center is produced below the cloud bridge. Thus, large amounts of new graupel and snow are generated, as well as a trace of ice and hail. Together with the upstream particles' transportation at the upper levels, more frequent collisions result in an increased electrification rate, which strengthens the charge density in the middle and downstream, generating the five-layer charge structure. A similar five-layer charge structure in the mature stage of a squall line was observed by a lightning detection network over BMR (Liu et al., 2013), which suggests the existence of such a five-layer charge structure and confirms the simulation results here, to some extent.

Generally, the balloon-borne in-situ measurements provide only a snapshot of the gross vertical charge structure of a storm and inferred storm charge from the state-of-the-art 3D lightning mapping technology reflects just the charge region involved in lightning discharges. The smaller scale or transient charge regions are impossible to observe with today's technology. In this study, a high spatiotemporal-resolution numerical simulation provides deeper insight into the evolution of charge distribution and lightning activity during a thunderstorm merger. In the future, lightning mapping results together with X-band dual-polarization radar data will be utilized to obtain the lightning-involved charge structure and the real microphysics distribution during the merger process, so that we can better understand how clouds interact and how the electrical activity is affected when they approach each other.

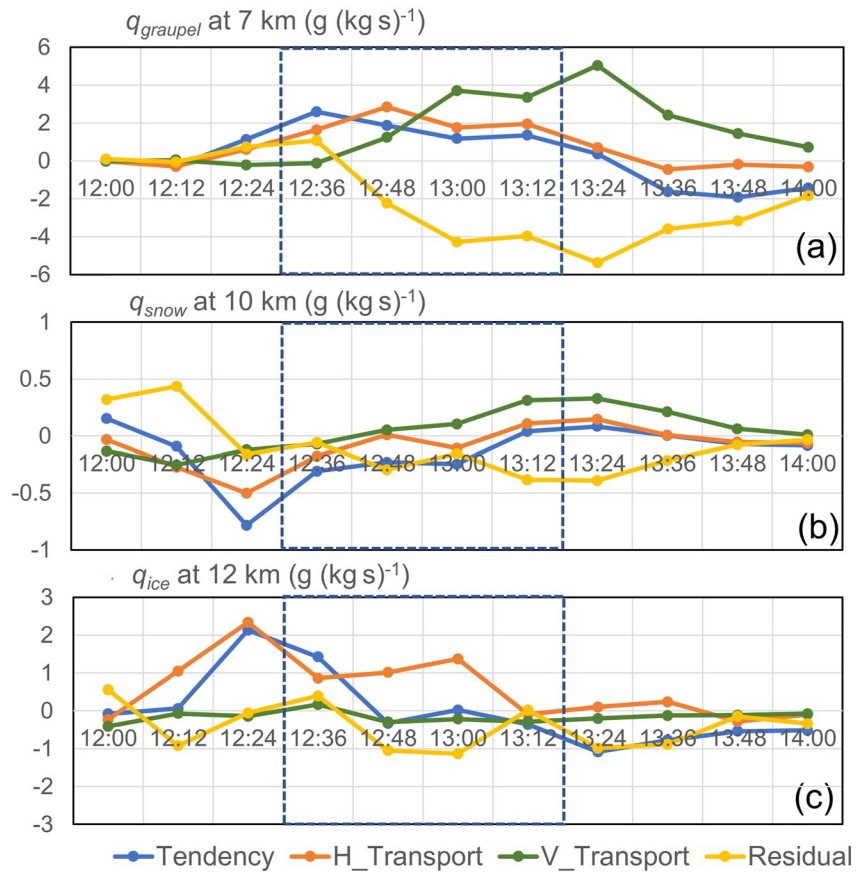


Figure 14. The variation of mixing ratios q_i per 12 min of Tendency (blue), the horizontal transport (H_Transport; orange), vertical transport (V_Transport; green), and residual term (yellow) of the ice-phase particle equation at (a) 7 km (graupel), (b) 10 km (snow), and (c) 12 km (ice). The convective merger is marked by the dashed blue lines.

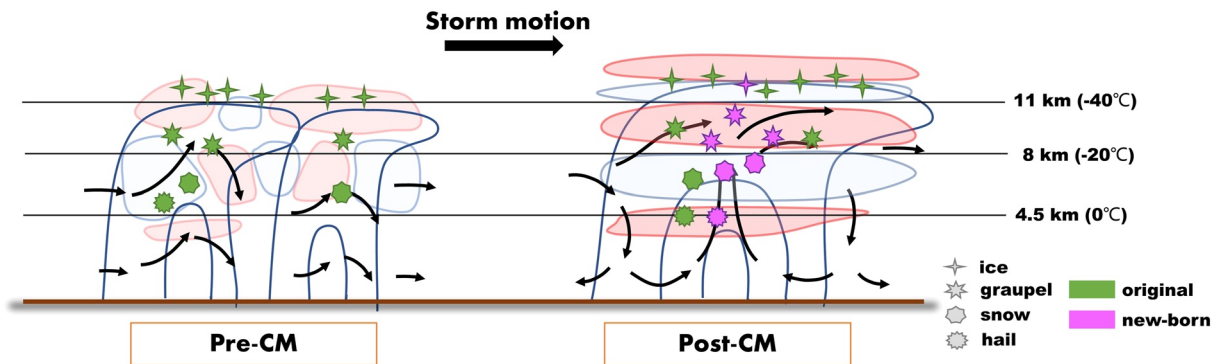


Figure 15. Conceptual diagram of thunderstorm dynamics, microphysics, and charge structure under the influence of the merging process.

Conflict of Interest

The authors declare no conflicts of interest relevant to this study.

Data Availability Statement

Reanalysis data are available from ERA-5, ECMWF (<https://www.ecmwf.int/en/forecasts/dataset/ecmwf-reanalysis-v5>). The WRF-*ELEC* source package for running *E*-WRF is made publicly available at <https://sourceforge.net/projects/wrfelec/> (Fierro et al., 2013; Mansell et al., 2005, 2010). The BLNET lightning data, radar data, and the *E*-WRF outputs can all be found in the Zenodo repository (<https://doi.org/10.5281/zenodo.6547800>; Lu, Qie, Xiao, et al., 2021). The figures were processed by Origin (version 2018, <https://www.originlab.com/>) and NCL (version 6.6.2, <https://www.ncl.ucar.edu/>), and the scripts can also be found in the Zenodo repository (<https://doi.org/10.5281/zenodo.6547800>; Lu, Qie, Xiao, et al., 2021).

Acknowledgments

The research was jointly supported by the National Natural Science Foundation of China (Grant nos. 41630425 and 41875008) and the National Natural Science Foundation of China in collaboration with the Israel Science Foundation (Grant nos. 41761144074 NSFC-ISF and 2640/17 ISF-NSFC). The authors are thankful for the effort of all the people who participated in coordinated observations of dynamic-microphysical-electrical processes in severe thunderstorms and lightning hazards. This work complies with the AGU data policy.

References

- Bang, S. D., & Zipser, E. (2019). Tropical oceanic thunderstorms near Kwajalein and the roles of evolution, organization, and forcing in their electrification. *Journal of Geophysical Research: Atmospheres*, *124*, 544–562. <https://doi.org/10.1029/2018JD029320>
- Bringi, V. N., Knupp, K., Detwiler, A., Liu, L., Caylor, I. J., & Black, R. A. (1997). Evolution of a Florida thunderstorm during the convection and precipitation/electrification experiment: The case of 9 August 1991. *Monthly Weather Review*, *125*(9), 2131–2160. [https://doi.org/10.1175/1520-0493\(1997\)125<2131:eoafid>2.0.co;2](https://doi.org/10.1175/1520-0493(1997)125<2131:eoafid>2.0.co;2)
- Brooks, I. M., Saunders, C. P. R., Mitzeva, R. P., & Peck, S. L. (1997). The effect on thunderstorm charging of the rate of rime accretion by graupel. *Atmospheric Research*, *43*, 277–295. [https://doi.org/10.1016/S0169-8095\(96\)00043-9](https://doi.org/10.1016/S0169-8095(96)00043-9)
- Carey, L. D., & Rutledge, S. A. (2000). The relationship between precipitation and lightning in tropical island convection: A C-band polarimetric radar study. *Monthly Weather Review*, *128*(8), 2687–2710. [https://doi.org/10.1175/1520-0493\(2000\)128<2687:trbpa>2.0.co;2](https://doi.org/10.1175/1520-0493(2000)128<2687:trbpa>2.0.co;2)
- Chakraborty, R., Chakraborty, A., Basha, G., & Ratnam, M. V. (2021). Lightning occurrences and intensity over the Indian region: Long-term trends and future projections. *Atmospheric Chemistry and Physics*, *21*, 11161–11177. <https://doi.org/10.5194/acp-2020-1280>
- Chen, Z., Qie, X., Yair, Y., Liu, D., Xiao, X., Wang, D., & Yuan, S. (2020). Electrical evolution of a rapidly developing MCS during its vigorous vertical growth phase. *Atmospheric Research*, *246*, 105201. <https://doi.org/10.1016/j.atmosres.2020.105201>
- Dafis, S., Fierro, A., Giannaros, T. M., Kotroni, V., Lagouvardos, K., & Mansell, E. (2018). Performance evaluation of an explicit lightning forecasting system. *Journal of Geophysical Research: Atmospheres*, *123*(10), 5130–5148. <https://doi.org/10.1029/2017JD027930>
- Dendy, J. E., Jr. (1987). Two multigrid methods for three-dimensional problems with discontinuous and anisotropic coefficients. *SIAM Journal on Scientific and Statistical Computing*, *8*(5), 673–685. <https://doi.org/10.1137/0908059>
- Dwyer, J. R. (2003). A fundamental limit on electric fields in air. *Geophysical Research Letters*, *30*(20), 2055. <https://doi.org/10.1029/2003gl017781>
- Feng, G., Qie, X., Yuan, T., & Niu, S. (2007). Analysis on lightning activity and precipitation structure of hailstorms. *Science in China - Series D: Earth Sciences*, *50*(4), 629–639. <https://doi.org/10.1007/s11430-007-2063-8>
- Feng, Z., Hagos, S., Rowe, A. K., Burleyson, C. D., Martini, M. N., & Szoek, S. P. (2015). Mechanisms of convective cloud organization by cold pools over tropical warm ocean during the AMIE/DYNAMO field campaign. *Journal of Advances in Modeling Earth Systems*, *7*, 357–381. <https://doi.org/10.1002/2014MS000384>
- Fierro, A. O., Gilmore, M. S., Mansell, E. R., Wicker, L. J., & Straka, J. M. (2006). Electrification and lightning in an idealized boundary-crossing supercell simulation of 2 June 1995. *Monthly Weather Review*, *134*(11), 3149–3172. <https://doi.org/10.1175/MWR3231.1>
- Fierro, A. O., Mansell, E. R., Macgorman, D. R., & Ziegler, C. L. (2013). Implementation of an explicit charging and discharge lightning scheme within the WRF-ARW model: Benchmark simulations of a continental squall line, a tropical cyclone, and a winter storm. *Monthly Weather Review*, *141*(7), 2390–2415. <https://doi.org/10.1175/MWR-D-12-00278.1>
- French, A. J., & Parker, M. D. (2012). Observations of mergers between squall lines and isolated supercell thunderstorms. *Weather and Forecasting*, *27*(2), 255–278. <https://doi.org/10.1175/WAF-D-11-00058.1>
- Gauthier, M. L., Petersen, W. A., & Carey, L. D. (2010). Cell mergers and their impact on cloud-to-ground lightning over the Houston area. *Atmospheric Research*, *96*(4), 626–632. <https://doi.org/10.1016/j.atmosres.2010.02.010>
- Glenn, I., & Krueger, S. K. (2017). Connections matter: Updraft merging in organized tropical deep convection. *Geophysical Research Letters*, *44*, 7087–7094. <https://doi.org/10.1002/2017GL074162>
- Haerter, J. O., & Schlemmer, L. (2018). Intensified cold pool dynamics under stronger surface heating. *Geophysical Research Letters*, *45*, 6299–6310. <https://doi.org/10.1029/2017GL076874>
- Karacostas, T., Spiridonov, V., Bampzelis, D., Pytharoulis, I., Tegoulas, I., & Tympanidis, K. (2016). Analysis and numerical simulation of a real cell merger using a three-dimensional cloud resolving model. *Atmospheric Research*, *169*, 547–555. <https://doi.org/10.1016/j.atmosres.2015.09.011>
- Keller, M., Fuhrer, O., Kröner, N., Lüthi, D., Schmidli, J., Stengel, M., et al. (2018). The sensitivity of alpine summer convection to surrogate climate change: An intercomparison between convection-parameterizing and convection-resolving models. *Atmospheric Chemistry and Physics*, *18*, 5253–5264. <https://doi.org/10.5194/acp-2017-504>
- Knievel, J. C., & Johnson, R. H. (2002). The kinematics of a midlatitude, continental mesoscale convective system and its mesoscale vortex. *Monthly Weather Review*, *130*(7), 1749–1770. [https://doi.org/10.1175/1520-0493\(2002\)130<1749:tkoamc>2.0.co;2](https://doi.org/10.1175/1520-0493(2002)130<1749:tkoamc>2.0.co;2)
- Knupp, K. R., Paech, S., & Goodman, S. (2003). Variations in cloud-to-ground lightning characteristics among three adjacent tornadic supercell storms over the Tennessee valley region. *Monthly Weather Review*, *131*(1), 172–188. [https://doi.org/10.1175/1520-0493\(2003\)131<0172:viactgl>2.0.co;2](https://doi.org/10.1175/1520-0493(2003)131<0172:viactgl>2.0.co;2)
- Krauss, T. W., Sin'kevich, A. A., & Ghulam, A. S. (2012). Radar investigations of cloud merger. *Russian Meteorology and Hydrology*, *37*(9), 604–614. <https://doi.org/10.3103/s106837391209004x>

- Lagasio, M., Parodi, A., Procopio, R., Rachidi, F., & Fiori, E. (2017). Lightning potential index performances in multimicrophysical cloud-resolving simulations of a back-building mesoscale convective system: The Genoa 2014 event. *Journal of Geophysical Research: Atmospheres*, 122(8), 4238–4257. <https://doi.org/10.1002/2016JD026115>
- Lenderink, G., Barbero, R., Loriaux, J. M., & Fowler, H. J. (2017). Super-Clausius–Clapeyron scaling of extreme hourly convective precipitation and its relation to large-scale atmospheric conditions. *Journal of Climate*, 30(15), 6037–6052. <https://doi.org/10.1175/JCLI-D-16-0808.1>
- Liu, D., Qie, X., Pan, L., & Liang, P. (2013). Some characteristics of lightning activity and radiation source distribution in a squall line over north China. *Atmospheric Research*, 132–133, 423–433. <https://doi.org/10.1016/j.atmosres.2013.06.010>
- Lu, J., Qie, X., Jiang, R., Xiao, X., Yi, X., Li, J., et al. (2021). Lightning activity during convective cell mergers in a squall line and corresponding dynamical and thermodynamical characteristics. *Atmospheric Research*, 256(8), 105555. <https://doi.org/10.1016/j.atmosres.2021.105555>
- Lu, J., Qie, X., Xiao, X., & Jiang, R. (2021). Effects of convective mergers on the evolution of microphysical and electrical activity in a severe squall line simulated by WRF coupled with explicit electrification scheme. [Data Set]. Zenodo. <https://doi.org/10.5281/zenodo.6547800>
- MacGorman, D. R., Filiaggi, T., Holle, R. L., & Brown, R. A. (2007). Negative cloud-to-ground lightning flash rates relative to VIL, maximum reflectivity, cell height, and cell isolation. *Journal of Lightning Research*, 1, 132–147.
- MacGorman, D. R., Straka, J. M., & Ziegler, C. L. (2001). A lightning parameterization for numerical cloud models. *Journal of Applied Meteorology and Climatology*, 40(3), 459–478. [https://doi.org/10.1175/1520-0450\(2001\)040<0459:alpfnc>2.0.co;2](https://doi.org/10.1175/1520-0450(2001)040<0459:alpfnc>2.0.co;2)
- Mansell, E. R., MacGorman, D. R., Ziegler, C. L., & Straka, J. M. (2005). Charge structure and lightning sensitivity in a simulated multicell thunderstorm. *Journal of Geophysical Research: Atmospheres*, 110(D12), D12101. <https://doi.org/10.1029/2004JD005287>
- Mansell, E. R., & Ziegler, C. L. (2013). Aerosol effects on simulated storm electrification and precipitation in a two-moment bulk microphysics model. *Journal of the Atmospheric Sciences*, 70, 2032–2050. <https://doi.org/10.1175/JAS-D-12-0264.1>
- Mansell, E. R., Ziegler, C. L., & Bruning, E. C. (2010). Simulated electrification of a small thunderstorm with two-moment bulk microphysics. *Journal of the Atmospheric Sciences*, 67, 171–194. <https://doi.org/10.1175/2009jas2965.1>
- Moseley, C., Henneberg, O., & Haerter, J. O. (2019). A statistical model for isolated convective precipitation events. *Journal of Advances in Modeling Earth Systems*, 11, 360–375. <https://doi.org/10.1029/2018MS001383>
- Moseley, C., Hohenegger, C., Berg, P., & Haerter, J. O. (2016). Intensification of convective extremes driven by cloud-cloud interaction. *Nature Geoscience*, 9(10), 748–752. <https://doi.org/10.1038/ngeo2789>
- Parker, M. D., & Johnson, R. H. (2004). Structures and dynamics of quasi-2D mesoscale convective systems. *Journal of the Atmospheric Sciences*, 61(5), 545–567. [https://doi.org/10.1175/1520-0469\(2004\)061<0545:sadoqm>2.0.co;2](https://doi.org/10.1175/1520-0469(2004)061<0545:sadoqm>2.0.co;2)
- Ping, F., Luo, Z., Tang, X., & Hu, L. (2014). A simulation of the merger of convective clouds in the torrential rainfalls associated with the Meiyu front. *Meteorology and Atmospheric Physics*, 123(1–2), 51–65. <https://doi.org/10.1007/s00703-013-0294-0>
- Qie, K., Qie, X., & Tian, W. (2021). Increasing trend of lightning activity in the South Asia region. *Science Bulletin*, 66, 78–84. <https://doi.org/10.1016/j.scib.2020.08.033>
- Qie, X., Yuan, S., Chen, Z., Wang, D., Liu, D., Sun, M., et al. (2020). Understanding the dynamical-microphysical-lightning processes associated with severe thunderstorms over the Beijing Metropolitan Region. *Science China Earth Sciences*, 63, 10–26. <https://doi.org/10.1007/s11430-020-9656-8>
- Romanic, D., LoTufio, J., & Hangan, H. (2019). Transient behavior in impinging jets in crossflow with application to downburst flows. *Journal of Wind Engineering and Industrial Aerodynamics*, 184, 209–227. <https://doi.org/10.1016/j.jweia.2018.11.020>
- Romps, D. M., Seeley, J. T., Vollaro, D., & Molinari, J. (2014). Projected increase in lightning strikes in the United States due to global warming. *Science*, 346(6211), 851–854. <https://doi.org/10.1126/science.1259100>
- Saunders, C. P. R., & Peck, S. L. (1998). Laboratory studies of the influence of the rime accretion rate on charge transfer during crystal/graupel collisions. *Journal of Geophysical Research*, 103(D12), 13949–13956. <https://doi.org/10.1029/97jd02644>
- Sinkevich, A. A., & Krauss, T. W. (2014). Changes in thunderstorm characteristics due to feeder cloud merging. *Atmospheric Research*, 142, 124–132. <https://doi.org/10.1016/j.atmosres.2013.06.007>
- Skamarock, W. C., & Klemp, J. B. (2007). A time-split nonhydrostatic atmospheric model for research and weather and forecasting. *Journal of Computational Physics*, 227, 3465–3485. <https://doi.org/10.1016/j.jcp.2007.01.037>
- Srivastava, A., Tian, Y., Qie, X., Wang, D., Sun, Z., Yuan, S., et al. (2017). Performance assessment of Beijing Lightning Network (BLNET) and comparison with other lightning location networks across Beijing. *Atmospheric Research*, 197, 76–83. <https://doi.org/10.1016/j.atmosres.2017.06.026>
- Stolzenburg, M., Rust, W. D., Stull, B. F., & Marshall, T. C. (1998). Electrical structure in thunderstorm convective regions: 1. Mesoscale convective systems. *Journal of Geophysical Research*, 103(D12), 14059–14078. <https://doi.org/10.1029/97jd03546>
- Sun, M., Liu, D., Qie, X., Mansell, E. R., Yair, Y., Fierro, A. O., et al. (2021). Aerosol effects on electrification and lightning discharges in a multicell thunderstorm simulated by the WRF-ELEC model. *Atmospheric Chemistry and Physics*, 21, 1–18. <https://doi.org/10.5194/acp-21-14141-2021>
- Takahashi, T., Yamaguchi, N., & Kawano, T. (2001). Videosonde observation of torrential rain during Baiu season. *Atmospheric Research*, 58(3), 205–228. [https://doi.org/10.1016/S0169-8095\(01\)00083-7](https://doi.org/10.1016/S0169-8095(01)00083-7)
- Tan, J., Jakob, C., Rossow, W. B., & Tselioudis, G. (2015). Increases in tropical rainfall driven by changes in frequency of organized deep convection. *Nature*, 519(7544), 451–454. <https://doi.org/10.1038/nature14339>
- Torri, G., & Kuang, Z. (2016). Rain evaporation and moist patches in tropical boundary layers. *Geophysical Research Letters*, 43, 9895–9902. <https://doi.org/10.1002/2016GL070893>
- Torri, G., Kuang, Z., & Tian, Y. (2015). Mechanisms for convection triggering by cold pools. *Geophysical Research Letters*, 42, 1943–1950. <https://doi.org/10.1002/2015GL063227>
- Wang, H., Liu, L., Xiao, Y., Zhuang, W., & Wang, G. (2009). Design and implementation of the CINRAD 3D digital mosaic system. *Meteorological Monographs*, 35(6), 13–18. <https://doi.org/10.7519/j.issn.1000-0526.2009.6.002>
- Wang, Y., Qie, X., Wang, D., Liu, M., Su, D., Wang, Z., et al. (2016). Beijing lightning network (BLNET) and the observation on preliminary breakdown processes. *Atmospheric Research*, 171, 121–132. <https://doi.org/10.1016/j.atmosres.2015.12.012>
- Wen, J., Zhao, K., Huang, H., Zhou, B., Yang, Z., Chen, G., et al. (2017). Evolution of microphysical structure of a subtropical squall line observed by a polarimetric radar and a disdrometer during OPACC in Eastern China. *Journal of Geophysical Research: Atmospheres*, 122, 8033–8050. <https://doi.org/10.1002/2016JD026346>
- Westcott, N. E. (1994). Merging of convective clouds: Cloud initiation, bridging, and subsequent growth. *Monthly Weather Review*, 122(5), 780–790. [https://doi.org/10.1175/1520-0493\(1994\)122<0780:moccci>2.0.co;2](https://doi.org/10.1175/1520-0493(1994)122<0780:moccci>2.0.co;2)
- Westra, S., Fowler, H., Evans, J., Alexander, L., Berg, P., Johnson, F., et al. (2014). Future changes to the intensity and frequency of short-duration extreme rainfall. *Reviews of Geophysics*, 52(3), 522–555. <https://doi.org/10.1002/2014RG000464>

- Xiao, X., Qie, X., Chen, Z., Lu, J., Ji, L., Wang, D., et al. (2021). Evaluating the performance of lightning data assimilation from BLNET observations in a 4DVAR-based Weather Nowcasting Model for a high-impact weather over Beijing. *Remote Sensing*, *13*(11), 2084. <https://doi.org/10.3390/rs13112084>
- Zheng, T. X., Tan, Y. B., & Wang, Y. R. (2021). Numerical simulation to evaluate the effects of upward lightning discharges on thunderstorm electrical parameters. *Advances in Atmospheric Sciences*, *38*(3), 446–459. <https://doi.org/10.1007/s00376-020-0154-z>
- Zhou, A., Zhao, K., Lee, W. C., Huang, H., Hu, D., & Fu, P. (2020). VDRAS and polarimetric radar investigation of a bow echo formation after a squall line merged with a preline convective cell. *Journal of Geophysical Research: Atmospheres*, *125*(7), e2019JD031719. <https://doi.org/10.1029/2019jd031719>
- Ziegler, C. L. (1985). Retrieval of thermal and microphysical variables in observed convective storms. Part I: Model development and preliminary testing. *Journal of the Atmospheric Sciences*, *42*(14), 1487–1509. [https://doi.org/10.1175/1520-0469\(1985\)042<1487:rotamv>2.0.co;2](https://doi.org/10.1175/1520-0469(1985)042<1487:rotamv>2.0.co;2)
- Ziegler, C. L., & MacGorman, D. R. (1994). Observed lightning morphology relative to modeled space charge and electric field distributions in a tornadic storm. *Journal of the Atmospheric Sciences*, *51*(6), 833–851. [https://doi.org/10.1175/1520-0469\(1994\)051<0833:olmrtm>2.0.co;2](https://doi.org/10.1175/1520-0469(1994)051<0833:olmrtm>2.0.co;2)
- Ziegler, C. L., MacGorman, D. R., Dye, J. E., & Ray, P. S. (1991). A model evaluation of noninductive graupel-ice charging in the early electrification of a mountain thunderstorm. *Journal of Geophysical Research*, *96*(D7), 12833–12855. <https://doi.org/10.1029/91jd01246>